Title

Differentiated roles of Lifshitz transition on thermodynamics and superconductivity in La2-xSrxCuO4

Journal

Proceedings of the National Academy of Sciences of the United States of America, 119(32)

ISSN

0027-8424

Authors

Zhong, Yong

Chen, Zhuoyu

Chen, Su-Di

et al.

Publication Date

2022-08-09

DOI

10.1073/pnas.2204630119

Peer reviewed

Differentiated roles of Lifshitz transition on thermodynamics and superconductivity in $La_{2-x}Sr_xCuO_4$

Yong Zhong[1,2,3†*], Zhuoyu Chen[1,3†*], Su-Di Chen[1,3], Ke-Jun Xu[1,3], Makoto Hashimoto[4], Yu He[5], Shin-ichi Uchida[6], Donghui Lu[4], Sung-Kwan Mo[2], and Zhi-Xun Shen[1,3*]

[1]*Stanford Institute for Materials and Energy Sciences, SLAC National Accelerator Laboratory, Menlo Park, CA 94025, USA*

[2]*Advanced Light Source, Lawrence Berkeley National Laboratory, Berkeley, CA 94720, USA*

[3]*Geballe Laboratory for Advanced Materials, Departments of Physics and Applied Physics, Stanford University, Stanford, CA 94305, USA*

[4]*Stanford Synchrotron Radiation Lightsource, SLAC National Accelerator Laboratory, Menlo Park, CA 94025, USA*

[5]*Department of Applied Physics, Yale University, New Haven, Connecticut 06511, USA*

[6]*Department of Physics, University of Tokyo, Tokyo 113-0033, Japan*

[*]Correspondence to: ylzhong@stanford.edu, zychen@stanford.edu, zxshen@stanford.edu

[†]These authors contributed equally.

The effect of a Lifshitz transition (LT) on thermodynamic properties and superconductivity in hole-doped cuprates has been heavily debated but remains an unanswered question. An observed maximum of electronic specific heat is proposed to originate from a quantum critical point associated with the LT. Here, we report an *in situ* angle-resolved photoemission spectroscopy study of the three-dimensional Fermi surfaces in $La_{2-x}Sr_xCuO_4$ thin films (x = 0.06 – 0.35). With accurate k_z dispersion quantification, the LT is determined to happen across a finite range x = 0.20 – 0.21. Normal state electronic specific heat, calculated from spectroscopy-derived band parameters, agrees with previous thermodynamic microcalorimetry measurements within experimental error. The quantitative account of the specific heat maximum by band structure effect excludes the need for additional contribution from quantum critical fluctuations. A *d*-wave superconducting gap smoothly evolving across the LT demonstrates the insensitivity of superconductivity to the LT associated density of states enhancement.

INTRODUCTION

The physics underlying the rich electronic phase diagram in hole-doped cuprates remains an active field of research [1-8]. With the change of doping, a Lifshitz transition (LT) of the Fermi surface is expected when the chemical potential crosses the van Hove singularity (VHS), at which point the Fermi surface transforms from a hole-like pocket around (π, π) to an electron-like pocket around (0, 0) [9]. Recent experimental reports, including the putative termination points of pseudogap [10], the putative quantum critical points seen in electronic specific heat and Hall number [11], and the anomalously low superfluid density in the electromagnetic response in over-doped regime [12,13], have attracted considerable attention. On the theoretical front, the presence of VHS was suggested to be important for the enhanced T_C and phase fluctuations [14-16]. Two-dimensional Hubbard model simulations proposed that this transition has a strong influence on the phase diagram of hole-doped cuprates [17-20]. For certain band structure parameters, the VHS was associated with a quantum critical point that changes the pairing symmetry of superconductivity [18,19]. Given the richness of experimental phenomenology and theoretical postulations, a systematic study of the electronic structure across the LT is desired.

Angle-resolved photoemission spectroscopy (ARPES) is a powerful tool to directly probe quantum material's Fermi surface in momentum space [21], yielding results that quantitatively agree with the results from transport quantum oscillations [22-25]. LTs have been studied in many types of cuprates by ARPES measurements, such as $La_{2-x}Sr_xCuO_4$ (LSCO) [26], $YBa_2Cu_3O_{6+\delta}$ (YBCO) [27], $(Bi,Pb)_2Sr_2CuO_{6+\delta}$ (Bi2201) [28] and $Bi_2Sr_2CaCu_2O_{8+\delta}$ (Bi2212) [29]. Among them, LSCO is an ideal platform because the p_{FS} in other cuprates are usually close to materials' doping solubility limit ($p_{FS} > 30\%$ in YBCO, $p_{FS} > 35\%$ in Bi2201, $p_{FS} > 29\%$ in Bi2212, but $p_{FS} < 22\%$ in LSCO). Nonetheless, the three dimensionality of LSCO extends the critical point p_{FS} to a finite range of dopings [30], within which "electron-like" and "hole-like" features coexist and manifest at different k_z. Therefore, a detailed doping-dependent and k_z-dependent photoemission study is needed to dissect the LT in LSCO.

Here, we utilize a recently developed oxide molecular-beam epitaxy system connected *in situ* to a synchrotron ARPES chamber, for the synthesis of LSCO thin films with precise control of thickness and doping levels (Fig. S1). Photon energy dependent ARPES measurements with improved spectral quality (Fig. S2) reveal an accurate out-of-plane hopping parameter, determining the LT range of doping $x = 0.20 - 0.21$. This is close to the doping of the normal-state electronic specific heat divergence and rapid Hall number change from p to $1+p$ in La-based cuprates [31,32]. With the band structure parameters determined by ARPES, we calculate the doping-dependent electronic specific heat at finite temperatures and found it quantitatively agreeing with previous thermodynamic microcalorimetry experiments [33] in the vicinity of LT. This provides a band structure explanation for the electronic specific heat maximum, without the need for additional contribution from a quantum critical point. We also perform momentum-dependent gap

measurement which shows persistent *d*-wave symmetry across the LT, with no enhancement of the gap magnitude near the VHS. Our finding is inconsistent with proposals that VHS or its associated critical fluctuations provide the direct pairing glue for high-temperature superconductivity.

RESULTS

Three-dimensional Fermi surface can be probed with in-plane momentum $\mathbf{k}_{||}$ (a combination of k_x and k_y) and out-of-plane momentum k_z. In ARPES measurements, we access these momenta through the following relations

$$\mathbf{k}_{\parallel} = \sqrt{2m(h\nu - \phi - E_B)}\sin\theta/\hbar, \tag{1}$$

$$k_z = \sqrt{2m(h\nu - \phi - E_B)\cos^2\theta + V_0}/\hbar, \tag{2}$$

where m is the electron mass, ϕ is the work function, E_B is the binding energy, θ is the polar angle, and V_0 is the inner potential. Firstly, as displayed in Fig. 1, we focus on the in-plane Fermi surface evolution at a selected photon energy $h\nu = 70\ eV$ (the selection of this photon energy will be discussed below). According to the Luttinger theorem, we calculate the doping levels via counting the filled states enclosed by the Fermi surface contours. In the following discussion, all the doping levels are determined by this method (Table S1 summarizes sample information). Secondly, we explore the out-of-plane Fermi surface by tuning the photon energies from 60 eV to 170 eV. A periodic k_F-k_z dispersion on the x = 0.22 sample is shown in Fig. 2A (for more details see Fig. S3). An inner potential V_0 = 9 eV is obtained via analyzing experimental data and considering the periodicity of Brillouin zones (BZ). We use momentum k_B at binding energy E_B = – 20 mV as a fingerprint to quantify the k_z dispersion. Sinusoidal-like k_B-k_z relation is observed along (π, 0) to (-π, 0) direction on both x = 0.22 and 0.35 samples, in contrast to the negligible variation along (0, 0) to (π, π) direction (Fig. 2B). We use a three-dimensional tight-binding model to fit the Fermi surfaces as a parameterization of the measured ARPES spectra [34]

$$\begin{aligned} E_{3D}(k_x, k_y, k_z) = &-\mu - 2t_1\left[\cos(k_x a) + \cos(k_y a)\right] - 4t_2\cos(k_x a)\cos(k_y a) \\ &-2t_3\left[\cos(2k_x a) + \cos(2k_y a)\right] \\ &-2t_z\cos\left(\frac{k_x a}{2}\right)\cos\left(\frac{k_y a}{2}\right)\cos\left(\frac{k_z c}{2}\right)\left[\cos(k_x a) - \cos(k_y a)\right]^2 \end{aligned} \tag{3}$$

Here t_1, t_2, and t_3 are the first, second, and third nearest neighbor hopping integrals between Cu sites. t_z represents the interlayer hopping coefficient. μ is the chemical potential. a is the in-plane lattice constant. $c/2$ is the distance between adjacent CuO_2 layers. In particular, the $\cos(k_x a/2)\cos(k_y a/2)[\cos(k_x a) - \cos(k_y a)]^2$ term accounts for the staggered stacking of neighboring CuO_2 planes in the body-centered tetragonal structure of LSCO [30]. Considering the universality of constant nodal Fermi velocity in a wide doping range of LSCO [35], we fix t_1 = 190 (± 15) meV (determined by fitting the nodal dispersions from

the Fermi level E_F to – 30 meV on all measured samples) and $t_3/t_2 = -0.5$ for all samples, and tune t_2, t_z and μ to depict the topography change of the Fermi surface (Table S2 summarizes all the parameters). The shift of μ is associated with the band filling effect from Sr dopants. The doping-dependent t_2 corresponds to a combined effect of structural change from chemical doping and electron correlation [36,37]. t_z can be obtained by fitting the experimental data via equation (3): $t_z = 0.03$ (± 0.01) t_1 on $x = 0.22$ sample, and $t_z = 0.04$ (± 0.01) t_1 on $x = 0.35$ sample, as shown in Fig. 2, A and B. $t_z = 0.04t_1$ is used to simulate the three-dimensional Fermi surfaces, as shown in the top right quadrant in each panel of Fig. 1. To quantify the LT regime accurately, we interpolate t_2 and μ linearly to obtain doping-dependent antinode's binding energy. This provides an estimated range of LT into $x = 0.20$ - 0.21 (the estimated width of the range is 0.007, with the error bar for x being 0.01), as shown in Fig. 2C. Same analysis for $t_z = 0.07t_1$ is also plotted for comparison [30]. The three-dimensional Fermi surface for $x = 0.22$ is illustrated in Fig. 2D, where the red contour denotes the in-plane Fermi surface at $h\nu = 70\ eV$. We selected this photon energy in Fig. 1 because the corresponding k_z locates at the midpoint between the largest and smallest Fermi surface, making it the most representative for the study of LT and doping level characterization.

Having characterized the LT in LSCO, we next examine its influence on the superconductivity. A typical Fermi surface map ($x = 0.22$) covering first and second BZs is shown in Fig. 3A, in which we selected an antinodal cut in the first BZ and a nodal cut in second BZ (for higher spectral intensity due to the matrix element effect in ARPES) as examples. The corresponding energy-momentum plots and energy distribution curves (EDC) are presented in Fig. 3 B to E. While no gap opening is found in node (Fig. 3C), there is a noticeable intensity depletion around E_F for the antinode (Fig. 3B), implying an anisotropic gap structure. Quantitative analysis of gap symmetry and magnitude in the superconducting state is shown in Fig. 4. As displayed in Fig. 4 A to D, we obtained gap size by fitting the symmetrized EDC at k_F with respect to E_F, with $A(\omega) = -1/\pi\ \mathrm{Im}(1/(\omega-\Sigma(\omega))$ and a constant background subtracted, where ω is the binding energy. The self-energy $\Sigma(\omega)$ can be expressed as $\Sigma(\omega) = -i\Gamma+\Delta^2/\omega$, where Γ is the single-particle scattering lifetime, and Δ is the superconducting gap at the Fermi momentum [38]. Gaussian convolution representing the instrumental resolution was applied to the spectral function. For overdoped films ($x = 0.17$, 0.22 and 0.24), symmetrized EDC at the antinode shows two coherence peaks with a gap opening. Moving from antinode towards node, the gap size decreases, and finally a single peak is observed at the node. Angle-dependent gap sizes are plotted in Fig. 4 E to H. Pure *d*-wave pairing symmetry is observed across the LT ($x = 0.17$, 0.22 and 0.24). For $x = 0.26$ and higher dopings, the gap is not detected in our measurements. On the underdoped side ($x = 0.12$), there is an obvious deviation of the antinodal gap from the nodal *d*-wave extrapolation, indicating the contribution of pseudogap in antinodal regime. This node-antinode dichotomy is a generic feature in underdoped cuprates [39-41].

DISCUSSION

The established three dimensionality of the Fermi surface is crucial for understanding the specific heat anomaly in LSCO. Microcalorimetry measurements of Nd-LSCO display a divergence of the normal-state electronic specific heat in the vicinity of LT [31], which was seen as a key signature to the existence of a quantum critical point inside the superconducting dome. The finite-temperature electronic specific heat coefficient is denoted as $\gamma = C_e/T$, where C_e is the electronic specific heat and T is the temperature. Theoretically, γ is the temperature derivative of total free fermion entropy S

$$S = k_B \int [-f ln f - (1-f) \ln (1-f)] \rho(E) dE. \quad (4)$$

Here f is the Fermi-Dirac function, k_B is the Boltzmann constant, and $\rho(E)$ represents the density of state (DOS) at binding energy E. Given that γ is closely related to the DOS near E_F, we calculate the doping-dependent $\rho(E)$ by an integration along the iso-energy surface:

$$\rho(E) = (1/4\pi^3) \int d\mathbf{k}/d\varepsilon(\mathbf{k}), \quad (5)$$

where $d\mathbf{k}$ is the volume element in momentum space. In the two-dimensional case, LT is associated with the divergence of DOS known as VHS, arising from the chemical potential crossing a saddle point at (π, 0), which also generates a significant anistropy of DOS along the Fermi surface (see Fig. S5 for details). In the LSCO system, three dimensionality reduces this divergence to a finite sharp peak. Below, we refer to this peak also as VHS for convenience.

In previous single crystal studies of LSCO, Nd-LSCO, and Eu-LSCO systems [30,31,42], the VHS was considered insufficient to account for the electronic specific heat anomaly. In our analysis above, we introduce doping-dependent t_2 and t_3 extracted directly from ARPES spectra, incorporating electron-correlation caused non-rigid band shift effect. Considering the updated band parameters and the smaller t_z we obtained, together with the temperature effect incorporated by equation (4), we revisit the relationship between VHS and the electronic specific heat. To directly compare our thin film results with previous single crystal results, we benchmark our thin film data by performing ARPES measurement on a x = 0.22 single crystal sample under the identical experimental setup, where we find similar Luttinger volume (= 22%), fitted band parameters, and t_z (= 0.04 ± 0.01 t_1) with the x = 0.22 thin film within experimental errors, as shown in Fig. S4.

Figure 5 displays the calculated γ based on the extracted band parameters from ARPES data (listed in Table S2). We compare the ARPES derived γ with the data from previous microcalorimetry measurements [33], revealing a marked consistency near and beyond the LT [43]. This quantitative agreement between the ARPES γ peak and the microcalorimetry γ peak within experimental errors excludes the necessity of the contribution from quantum critical fluctuations in the LSCO system. The deviation in underdoped side may be related to the pseudogap formation and the existence of charge orders [11]. For the Nd-LSCO and Eu-LSCO cases, quantum critical fluctuations could be at play for a sharper γ peak [31], but the lower T_C

in these cation-substituted systems compared with LSCO indicate that the quantum critical fluctuations, if exist, may have little correlation with superconductivity. We note that similar observations and analysis of VHS were reported in strontium ruthenates [44-46].

Except for the divergent behavior of γ, there are other experimental observations pointing to a putative quantum critical point in cuprates. One of them is the rapid Hall number change from p to $1+p$ at the pseudogap endpoint in Nd-LSCO and YBCO [32,47], perhaps corresponding to a LT across the critical point. However, recent transport experiments display a smooth p to $1+p$ transition over a wide range of doping in Tl2201 and Bi2201 [48], which implies that the sharp change of Hall effect at the putative pseudogap critical point is not a universal feature in cuprates. Furthermore, systematic photoemission antinodal data exhibit a sharp vertical boundary up to room temperature and beyond, implying a different kind of transition than the putative quantum critical point [49].

Finally, we discuss the role of LT on superconductivity. Our results show that the VHS with significantly enhanced DOS has little effect on both the superconducting gap size and gap symmetry in the LSCO system. In Bi2201 and Bi2212, the LT is found experimentally coinciding with the overdoped endpoint of superconductivity. This correlation has been considered as a possible interpretation for the disappearance of superconductivity in overdoped cuprates. Dynamical cluster approximation calculation [18] displayed a spin susceptibility transition from antiferromagnetic type peaked at $q = (\pi, \pi)$ to ferromagnetic type centered at $q = (0,0)$ across the critical point p_{FS}. In addition, renormalization group analysis [19] and quantum Monte Carlo simulation [50] both predicted the existence of ferromagnetic fluctuations at van Hove filling in two-dimensional Hubbard model, which has been observed recently in heavily overdoped *p*-type and *n*-type cuprates [51,52]. We have shown that LSCO system manifests robust *d*-wave superconductivity across the LT, and the transition point p_{FS} is far lower than the SC endpoint, incompatible with the theoretical prediction of triplet *p*-wave pairing beyond the LT. An alternative theoretical proposal to the reduced superconductivity is that the flat band dispersion near the antinode makes the *d*-wave pairing amplitude and phase coherence sensitive to impurity concentrations that increase with *x* [53-55].

In conclusion, by systematic ARPES measurements on LSCO thin films, we accurately determined the doping range where the LT occurs. We found a quantitative consistency between electronic specific heat calculated from ARPES band parameters and that from previous thermodynamic measurements in the vicinity of LT. These results show that in the LSCO system, the putative quantum critical point is not needed to account for the amplitude of the electronic specific heat peak. We further unambiguously show that the superconducting gap remains persistently *d*-wave symmetry with no obvious enhancement of size on both sides of the LT. Our results reveal the differentiated roles of LT and the associated enhanced DOS on thermodynamic properties and superconductivity in LSCO: the LT causes the electronic specific heat peak but has almost no effect on superconducting gap size and symmetry.

MATERIALS AND METHODS

$La_{2-x}Sr_xCuO_4$ thin films with x = 0.06, 0.12, 0.17, 0.22, 0.26, 0.31, and 0.35 were synthesized on $LaSrAlO_4$ (001) substrates in a Veeco GEN930 MBE system with continuous supply of purified ozone. The growth process was monitored by in situ reflective high energy electron diffraction (RHEED). Metal sources are individually shuttered to realize an atomic-layer-by-layer control of the growth, ensuring an atomically flat surface without impurities for optimized ARPES measurements. All samples presented in this work were 13.3 nm thick (10 unit cells) with LaO termination. The growth was performed at 700 ºC, under background pressure of 1×10^{-5} Torr of purified ozone. After the growth, the sample was immediately transferred under ultra-high vacuum to the ARPES end station at Stanford Synchrotron Radiation Lightsource beamline 5-2 equipped with a Scienta DA30 analyzer. The base pressure during the ARPES measurements was better than 3×10^{-11} Torr. Linear-horizontally polarized light with $h\nu$ = 70 eV was used to map the Fermi surface and detect the gap structure. Measurement temperature was 9 K, and the energy resolution was 12 meV. The k_z dispersion was studied within a photon energy range 60 – 150 eV and at a temperature of 150 K. Previous report that found a reasonable agreement between the quasiparticle estimation and the experiment of Luttinger liquid specific heat [56] inspire our use of band parameters to derive and compare with specific heat data in LSCO. We use fitted band parameters from the entire Fermi to calculate the Fermi velocity and the associated density of states as described in the main text, since it is better constrained with lower error level than local extractions [42], especially for the antinode regime. More details about the growth and measurement are shown in Supplementary Material.

REFERENCES AND NOTES

[1] B. Keimer, S. A. Kivelson, M. R. Norman, S. Uchida, and J. Zaanen, From quantum matter to high-temperature superconductivity in copper oxides, *Nature* ***518***, 179 (2015).

[2] A. Damascelli, Z. Hussain, and Z. X. Shen, Angle-resolved photoemission studies of the cuprate superconductors, *Rev. Mod. Phys.* ***75***, 473 (2003).

[3] T. Timusk, and B. Statt, The pseudogap in high-temperature superconductors: an experimental survey, *Rep. Prog. Phys.* ***62***, 61 (1999).

[4] M. R. Norman, D. Pines, and C. Kallin, The pseudogap: friend or foe of high T_C? *Adv. Phys.* ***54***, 715 (2005).

[5] C. M. Varma, P. B. Littlewood, S. Schmitt-Rink, E. Abrahams, and A. E. Ruckenstein, Phenomenology of the normal state of Cu-O high-temperature superconductors, *Phys. Rev. Lett.* ***63***, 1996 (1989).

[6] S. A. Hartnoll, J. Polchinski, E. Silverstein, and D. Tong, Towards strange metallic holography, *J. High Energy Phys.* ***4***, 1 (2010).

[7] E. Fradkin, S. A. Kivelson, and J. M. Tranquada, *Colloquium*: Theory of intertwined orders in high temperature superconductors, *Rev. Mod. Phys.* ***87***, 457 (2015).

[8] R. Comin, and A. Damascelli, Resonant X-ray scattering studies of charge order in cuprates, *Annu. Rev. Condens. Matter Phys.* ***7***, 369 (2016).

[9] W. E. Pickett, Electronic structure of the high-temperature oxide superconductors, *Rev. Mod. Phys.* ***61***, 433 (1989).

[10] N. Doiron-Leyraud, O. Cyr-Choinière, S. Badoux, A. Ataei, C. Collignon, A. Gourgout, S. Dufour-Beauséjour, F. F. Tafti, F. Laliberté, M.-E. Boulanger, M. Matusiak, D. Graf, M. Kim, J.-S. Zhou, N. Momono, T. Kurosawa, H. Takagi, and L. Taillefer, Pseudogap phase of cuprate superconductors confined by Fermi surface topology. *Nat. Commun.* ***8***, 2044 (2017).

[11] C. Proust, and L. Taillefer, The remarkable underlying ground states of cuprate superconductors, *Annu. Rev. Condens. Matter Phys.* ***10***, 409 (2019).

[12] I. Božović, X. He, J. Wu, and A. T. Bollinger, Dependence of the critical temperature in overdoped copper oxides on superfluid density, *Nature* ***536***, 309 (2016).

[13] F. Mahmood, X. He, I. Božović, and N. P. Armitage, Locating the missing superconducting electrons in the overdoped cuprates $La_{2-x}Sr_xCuO_4$, *Phys. Rev. Lett.* ***122***, 027003 (2019).

[14] R. S. Markiewicz, A survey of the van Hove scenario for high-T_C superconductivity with special emphasis on pseudogaps and striped phases, *J. Phys. Chem. Solids* ***58***, 1179 (1997).

[15] C. C. Tsuei, D. M. Newns, C. C. Chi, and P. C. Pattnaik, Anomalous isotope effect and van Hove singularity in superconducting Cu oxides, *Phys. Rev. Lett.* ***65***, 2724 (1990).

[16] Y. He, S. D. Chen, Z. X. Li, D. Zhao, D. Song, Y. Yoshida, H. Eisaki, T. Wu, X. H. Chen, D. H. Lu, C. Meingast, T. P. Devereaux, R. J. Birgeneau, M. Hashimoto, D. H. Lee, and Z. X. Shen, Superconducting fluctuations in overdoped $Bi_2Sr_2CaCu_2O_{8+\delta}$, *Phys. Rev. X* ***11***, 031068 (2021).

[17] W. Wu, M. S. Scheurer, S. Chatterjee, S. Sachdev, A. Georges, and M. Ferrero, Pseudogap and Fermi-surface topology in the two-dimensional Hubbard model, *Phys. Rev. X* ***8***, 021048 (2018).

[18] T. A. Maier, S. Karakuzu, and D. J. Scalapino, Overdoped end of the cuprate phase diagram, *Phys. Rev. Res.* ***2***, 033132 (2020).

[19] C. Honerkamp, and M. Salmhofer, Magnetic and superconducting instabilities of the Hubbard model at the van Hove filling, *Phys. Rev. Lett.* ***87***, 187004 (2001).

[20] K. S. Chen, Z. Y. Meng, T. Pruschke, J. Moreno, and M. Jarrell, Lifshitz transition in the two-dimensional Hubbard model, *Phys. Rev. B* ***86***, 165136 (2012).

[21] J. A. Sobota, Y. He, and Z. X. Shen, Angle-resolved photoemission studies on quantum materials, *Rev. Mod. Phys.* ***93***, 025006 (2021).

[22] M. Platé, J. D. F. Mottershead, I. S. Elfimov, D. C. Peets, R. Liang, D. A. Bonn, W. N. Hardy, S. Chiuzbaian, M. Falub, M. Shi, L. Patthey, and A. Damascelli, Fermi surface and quasiparticle excitations of overdoped $Tl_2Ba_2CuO_{6+\delta}$, *Phys. Rev. Lett.* ***95***, 077001 (2005).

[23] N. E. Hussey, M. Abdel-Jawad, A. Carrington, A. P. Mackenzie, and L. Balicas, A coherent three-dimensional Fermi surface in a high-transition-temperature superconductor, *Nature* ***425***, 814 (2003).

[24] J. F. He, C. R. Rotundu, M. S. Scheurer, Y. He, M. Hashimoto, K. J. Xu, Y. Wang, E. W. Huang, T. Jia, S. D. Chen, B. Moritz, D. H. Lu, Y. S. Lee, T. P. Devereaux, and Z. X. Shen, Fermi surface reconstruction in electron-doped cuprates without antiferromagnetic long-range order, *Proc. Natl. Acad. Sci. U.S.A.* ***116***, 3449 (2019).

[25] T. Helm, M. V. Kartsovnik, M. Bartkowiak, N. Bittner, M. Lambacher, A. Erb, J. Wosnitza, and R. Gross, Evolution of the Fermi surface of the electron-doped high-temperature superconductor $Nd_{2-x}Ce_xCuO_4$ revealed by Shubnikov-de Haas oscillations, *Phys. Rev. Lett.* ***103***, 157002 (2009).

[26] T. Yoshida, X. J. Zhou, K. Tanaka, W. L. Yang, Z. Hussain, Z. X. Shen, A. Fujimori, S. Sahrakorpi, M. Lindroos, R. S. Markiewicz, A. Bansil, S. Komiya, Y. Ando, H. Eisaki, T. Kakeshita, and S. Uchida, Systematic doping evolution of the underlying Fermi surface of $La_{2-x}Sr_xCuO_4$, *Phys. Rev. B* ***74***, 224510 (2006).

[27] V. B. Zabolotnyy, S. V. Borisenko, A. A. Kordyuk, J. Geck, D. S. Inosov, A. Koitzsch, J. Fink, M. Knupfer, B. Büchner, S. L. Drechsler, H. Berger, A. Erb, M. Lambacher, L. Patthey, V. Hinkov, and B. Keimer, Momentum and temperature dependence of renormalization effects in high-temperature superconductor $YBa_2Cu_3O_{7-\delta}$, *Phys. Rev. B* ***76***, 064519 (2007).

[28] T. Kondo, T. Takeuchi, T. Yokoya, S. Tsuda, S. Shin, and U. Mizutani, Hole-concentration dependence of band structure in $(Bi,Pb)_2(Sr,La)_2CuO_{6+\delta}$ determined by the angle-resolved photoemission spectroscopy, *J. Electron Spectrosc. Relat. Phenom.* ***137***, 663 (2004).

[29] I. K. Drozdov, I. Pletikosić, C.-K. Kim, K. Fujita, G. D. Gu, J. C. Séamus Davis, P. D. Johnson, I. Božović, and T. Valla, Phase diagram of $Bi_2Sr_2CaCu_2O_{8+\delta}$ revisited, *Nat. Commun.* ***9***, 5210 (2018).

[30] M. Horio, K. Hauser, Y. Sassa, Z. Mingazheva, D. Sutter, K. Kramer, A. Cook, E. Nocerino, O. K. Forslund, O. Tjernberg, M. Kobayashi, A. Chikina, N. B. M. Schröter, J. A. Krieger, T Schmitt, V. N. Strocov, S. Pyon, T. Takayama, H. Takagi, O. J. Lipscombe, S. M. Hayden, M. Ishikado, H. Eisaki, T. Neupert, M. Månsson, C. E. Matt, and J. Chang, Three-dimensional Fermi surface of overdoped La-based cuprates, *Phys. Rev. Lett.* ***121***, 077004 (2018).

[31] B. Michon, C. Girod, S. Badoux, J. Kačmarčík, Q. Ma, M. Dragomir, H. A. Dabkowska, B. D. Gaulin, J. S. Zhou, S. Pyon, T. Takayama, H. Takagi, S. Verret, N. Doiron-Leyraud, C. Marcenat, L. Taillefer, and

T. Klein, Thermodynamic signatures of quantum criticality in cuprate superconductors, *Nature* ***567***, 218 (2019).

[32] C. Collignon, S. Badoux, S. A. A. Afshar, B. Michon, F. Labiberté, O. Cyr-Choinière, J. S. Zhou, S. Licciardello, S. Wiedmann, N. Doiron-Leyraud, and L. Taillefer, Fermi-surface transformation across the pseudogap critical point of the cuprate superconductor $La_{1.6-x}Nd_{0.4}Sr_xCuO_4$, *Phys. Rev. B* ***95***, 224517 (2017).

[33] C. Girod, D. LeBoeuf, A. Demuer, G. Seyfarth, S. Imajo, K. Kindo, Y. Kohama, M. Lizaire, A. Legros, A. Gourgout, H. Takagi, T. Kurosawa, M. Oda, N. Momono, J. Chang, S. Ono, G. Q. Zheng, C. Marcenat, L. Taillefer, and T. Klein, Normal state specific heat in the cuprate superconductors $La_{2-x}Sr_xCuO_4$ and $Bi_{2+y}Sr_{2-x-y}La_xCuO_{6+\delta}$ near the critical point of the pseudogap phase, *Phys. Rev. B* ***103***, 214506 (2021).

[34] S. Sahrakorpi, M. Lindroos, R. S. Markiewicz, and A. Bansil, Evolution of midgap states and residual three dimensionality in $La_{2-x}Sr_xCuO_4$, *Phys. Rev. Lett.* ***95***, 157601 (2005).

[35] X. J. Zhou, T. Yoshida, A. Lanzara, P. V. Bogdanov, S. A. Kellar, K. M. Shen, W. L. Yang, F. Ronning, T. Sasagawa, T. Kakeshita, T. Noda, H. Eisaki, S. Uchida, C. T. Lin, F. Zhou, J. W. Xiong, W. X. Ti, Z. X. Zhao, A. Fujimori, Z. Hussain, and Z. X. Shen, Universal nodal Fermi velocity, *Nature* ***423***, 398 (2003).

[36] E. Pavarini, I. Dasgupta, T. Saha-Dasgupta, O. Jepsen, and O. K. Andersen, Band-structure trend in hole-doped cuprates and correlation with T_{cmax}, *Phys. Rev. Lett.* ***87***, 047003 (2001).

[37] M. Civelli, M. Capone, S. S. Kancharla, O. Parcollet, and G. Kotliar, Dynamical breakup of the Fermi surface in a doped Mott insulator, *Phys. Rev. Lett.* ***95***, 106402 (2005).

[38] M. R. Norman, M. Randeria, H. Ding, and J. C. Campuzano, Phenomenology of the low-energy spectral function in high-T_C superconductors, *Phys. Rev. B* ***57***, R11093 (1998).

[39] W. S. Lee, I. M. Vishik, K. Tanaka, D. H. Lu, T. Sasagawa, N. Nagaosa, T. P. Devereaux, Z. Hussain and Z. X. Shen, Abrupt onset of a second energy gap at the superconducting transition of underdoped Bi2212, *Nature* ***450***, 81 (2007).

[40] T. Kondo, T. Takeuchi, A. Kaminski, S. Tsuda, and S. Shin, Evidence for two energy scales in the superconducting state of optimally doped $(Bi, Pb)_2(Sr, La)_2CuO_{6+\delta}$, *Phys. Rev. Lett.* ***98***, 267004 (2007).

[41] T. Yoshida, M. Hashimoto, S. Ideta, A. Fujimori, K. Tanaka, N. Mannella, Z. Hussain, Z. X. Shen, M. Kubota, K. Ono, S. Komiya, Y. Ando, H. Eisaki, and S. Uchida, Universal versus material-dependent two-gap behaviors of the high-Tc cuprate superconductors: angle-resolved photoemission study of $La_{2-x}Sr_xCuO_4$, *Phys. Rev. Lett.* ***103***, 037004 (2009).

[42] T. Yoshida, X. J. Zhou, D. H. Lu, S. Komiya, Y. Ando, H. Eisaki, T. Kakeshita, S. Uchida, Z. Hussain, Z. X. Shen, and A. Fujimori, Low-energy electronic structure of the high-T_C cuprates $La_{2-x}Sr_xCuO_4$ studied by angle-resolved photoemission spectroscopy, *J. Phys.: Condens. Matter* ***19***, 125209 (2007).

[43] G. Grissonnanche, Y. Fang, A. Legros, S. Verret, F. Laliberté, C. Collignon, J. Zhou, D. Graf, P. A. Goddard, L. Taillefer, and B. J. Ramshaw, *Nature* ***595***, 667–672 (2021).

[44] S. A. Grigera, R. S. Perry, A. J. Schofield, M. Chiao, S. R. Julian, G. G. Lonzarich, S. I. Ikeda, Y. Maeno, A. J. Millis, and A. P. Mackenzie, Magnetic field-tuned quantum criticality in the metallic ruthenate $Sr_3Ru_2O_7$, *Science* ***294***, 329 (2001).

[45] A. Tamai, M. P. Allan, J. F. Mercure, W. Meevasana, R. Dunkel, D. H. Lu, R. S. Perry, A. P. Mackenzie, D. J. Singh, Z. X. Shen, and F. Baumberger, Fermi surface and van Hove singularities in the itinerant metamagnet $Sr_3Ru_2O_7$, *Phys. Rev. Lett.* ***101***, 026407 (2008).

[46] C. H. Mousatov, E. Berg, and S. A. Hartnoll, Theory of the strange metal $Sr_3Ru_2O_7$, *Proc. Natl. Acad. Sci. U.S.A.* ***117***, 2852 (2020).

[47] S. Badoux, W. Tabis, F. Laliberté, G. Grissonnanche, B. Vignolle, D. Vignolles, J. Béard, D. A. Bonn, W. N. Hardy, R. Liang, N. Doiron-Leyraud, L. Taillefer, and C. Proust, Change of carrier density at the pseudogap critical point of a cuprate superconductor, *Nature* ***531***, 210 (2016).

[48] C. Putzke, S. Benhabib, W. Tabis, J. Ayres, Z. Wang, L. Malone, S. Licciardello, J. Lu, T. Kondo, T. Takeuchi, N. E. Hussey, J. R. Cooper, and A. Carrington, Reduced Hall carrier density in the overdoped strange metal regime of cuprate superconductors, *Nat. Phys.* ***17***, 826 (2021).

[49] S. D. Chen, M. Hashimoto, Y. He, D. Song, K. J. Xu, J. F He, T. P. Devereaux, H. Eisaki, D. H. Lu, J. Zaanen, and Z. X. Shen, Incoherent strange metal sharply bounded by a critical doping in Bi2212, *Science* ***366***, 1099 (2019).

[50] R. Hlubina, S. Sorella, and F. Guinea, Ferromagnetism in the two-dimensional t-t' Hubbard model at the van Hove density, *Phys. Rev. Lett.* ***78***, 1343 (1997).

[51] K. Kurashima, T. Adachi, K. M. Suzuki, Y. Fukunaga, T. Kawamata, T. Noji, H. Miyasaka, I. Watanabe, M. Miyazaki, A. Koda, R. Kadono, and Y. Koike, Development of ferromagnetic fluctuations in heavily overdoped $(Bi, Pb)_2Sr_2CuO_{6+\delta}$ copper oxides, *Phys. Rev. Lett.* ***121***, 057002 (2018).

[52] T. Sarkar, D. S. Wei, J. Zhang, N. R. Poniatowski, P. R. Mandal, A. Kapitulnik, and R. L. Greene, Ferromagnetic order beyond the superconducting dome in a cuprate superconductor, *Science* ***368***, 532 (2020).

[53] N. R. Lee-Hone, V. Mishra, D. M. Broun, and P. J. Hirschfeld, Optical conductivity of overdoped cuprate superconductors: application to $La_{2-x}Sr_xCuO_4$, *Phys. Rev. B* ***98***, 054506 (2018).

[54] Z. X. Li, S. A. Kivelson, and D. H. Lee, Superconductor-to-metal transition in overdoped cuprates, *npj Quantum Mater.* ***6***, 36 (2021).

[55] G. Kim, K. S. Rabinovich, A. V. Boris, A. N. Yaresko, Y. E. Suyolcu, Y. M. Wu, P. A. van Aken, G. Christiani, G. Logvenov, and B. Keimer, Optical conductivity and superconductivity in highly overdoped $La_{2-x}Ca_xCuO_4$ thin films, *Proc. Natl. Acad. Sci. U.S.A.* ***118***, e2106170118 (2021).

[56] M. Hagiwara, H. Tsujii, C. R. Rotundu, B. Andraka, Y. Takano, N. Tateiwa, T. C. Kobayashi, T. Suzuki, and S. Suga, Tomonaga-luttinger liquid in a quasi-one-dimensional s= 1 antiferromagnet observed by specific heat measurements, *Phys. Rev. Lett.* **96**, 147203 (2006).

Acknowledgements

We thank S. A. Kivelson, D. H. Lee, T. P. Devereaux, D. J. Scalapino, P. J. Hirschfeld, and E. Huang for stimulating discussions. ARPES experiments were performed at Beamline 5-2, Stanford Synchrotron Radiation Lightsource, SLAC National Accelerator Laboratory. **Funding:** This work was supported by the U.S. Department of Energy, Office of Science, Office of Basic Energy Sciences, Materials Sciences and Engineering Division, under Contract DE-AC02-76SF00515. The work at ALS, LBNL was supported by US DOE under contract No. DE-AC02-05CH11231. **Author contributions:** Y.Z. and Z.C. grew the films, performed ARPES measurements, and analyzed data. S.D.C. and K.J.X. assisted in ARPES measurement and data analysis. M.H. and D.L. developed the ARPES setup and assisted in ARPES measurements. S.K.M. and Y.H. participated in discussions. S.U. provided the single crystal samples. Z.C. and Z.X.S. conceived the experiment. Y.Z., Z.C., and Z.X.S. wrote the manuscript with input from all authors. Z.X.S. supervised the project. **Competing interests:** The authors declare no competing interests. **Data and materials availability:** All data needed to evaluate the conclusions in the paper are present in the paper and/or the Supplementary Materials.

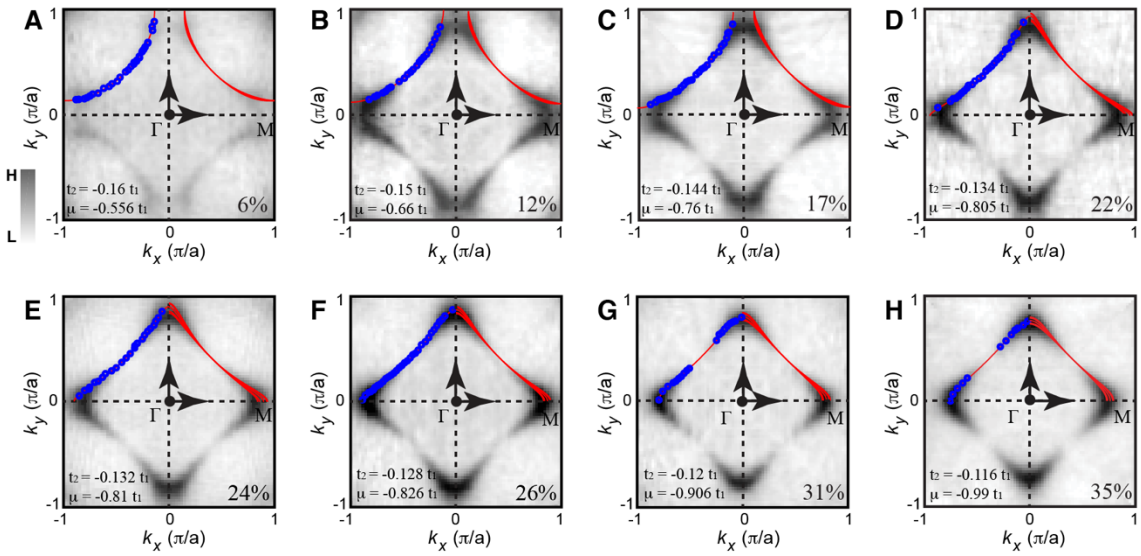

Fig. 1. **Three-dimensional Fermi surface projected onto k_x-k_y plane.** (A-H) Doping-dependent in-plane Fermi surface maps. All the Fermi surfaces are integrated within the spectral weight window E_F ± 5 meV (x = 0.06 sample with E_F ± 25 meV due to the low intensity near E_F) and four-fold symmetrized in first Brillouin zone. Fermi momentum k_F (blue circles) is determined by the peaks of the corresponding momentum distribution curves (MDC) at E_F. Red curves on top left quadrant of Brillouin zone are simulating in-plane Fermi surfaces at $k_z = \pi/c\,(h\nu = 70eV)$. Red curves on top right quadrant of Brillouin zone are simulating three-dimensional Fermi surfaces projected onto k_x-k_y plane. We use t_z = 0.04 t_1 for all simulations. Doping levels were determined by Luttinger theorem. Measurement temperature is 9 K. Details of band structure parameters t_1, t_2, t_3 and μ are listed in Table S1.

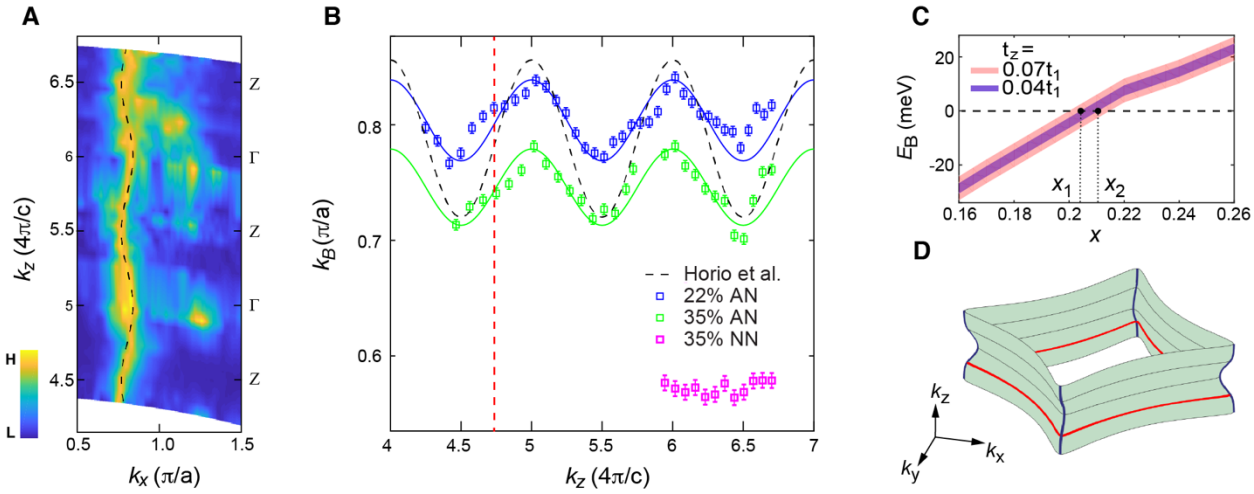

Fig. 2. **Three-dimensional Fermi surface projected onto k_x-k_z plane.** (A) Out-of-plane Fermi surface maps along antinodal (π, 0) direction for x = 0.22 sample. Photon energies are swept in the range 60 – 150 eV to cut different k_z planes. (B) k_B - k_z dispersion along antinodal (π, 0) direction for x = 0.22 sample (blue squares), and along (anti)nodal (π, 0)/(π, π) directions for x = 0.35 sample (green and magenta squares). k_B is the momentum located at the energy contour E = – 20 mV. Error bars denotes the uncertainty to obtain k_B. The blue and green lines represent the three-dimensional tight-binding simulations. The black dashed line is a reference [30]. Red dashed line is the corresponding k_z at photon energy $h\nu = 70eV$. (C) Doping dependent binding energy E_B at the antinodal momentum k = (0.98 π, 0.02 π). Results from two interlayer hopping parameters (t_z = 0.04 t_1, 0.07 t_1) are shown. Smaller t_z narrows the Lifshitz transition regime to x = 0.20 – 0.21. Violet and red areas represent the binding energy range for the two different k_z, respectively. x_1 and x_2 are the lower and upper bounds of the Lifshitz transition range. (D) Three-dimensional Fermi surface illustration of LSCO at x = 0.22. The red contour is the in-plane Fermi surface at $k_z = \pi/c$. Measurement temperature is 150 K.

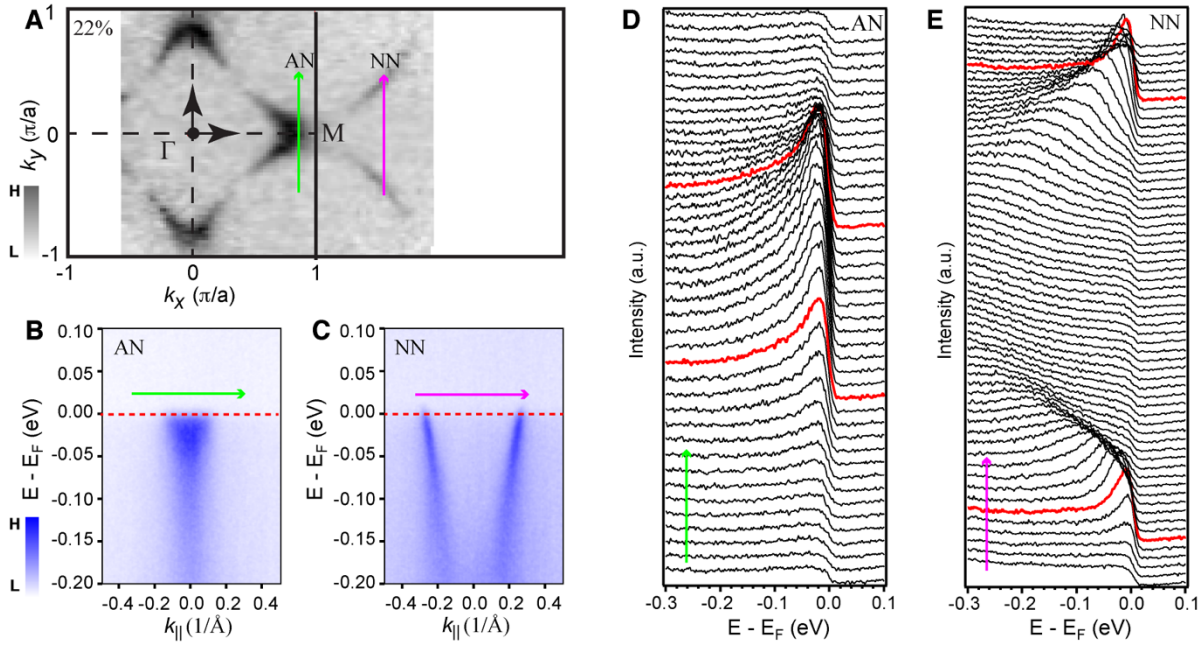

Fig. 3. **Low-energy electronic structure of LSCO at x = 0.22.** (A) In-plane Fermi surface map covering 1st and 2nd BZs. Due to the matrix element effect, we measure antinodal spectra in 1st Brillouin zone, and nodal spectra at 2nd Brillouin zone. (B,C) Energy-momentum spectra along antinodal (green arrow) and nodal (magenta arrow) cuts. Red dashed line denotes the Fermi level. (D,E) The corresponding EDC curves along antinodal and nodal cuts labelled by green and magenta arrows respectively. Red curves are the EDCs at Fermi momenta k_F's. k_F in D is determined by the minimum gap criterion. Measurement temperature is 9 K.

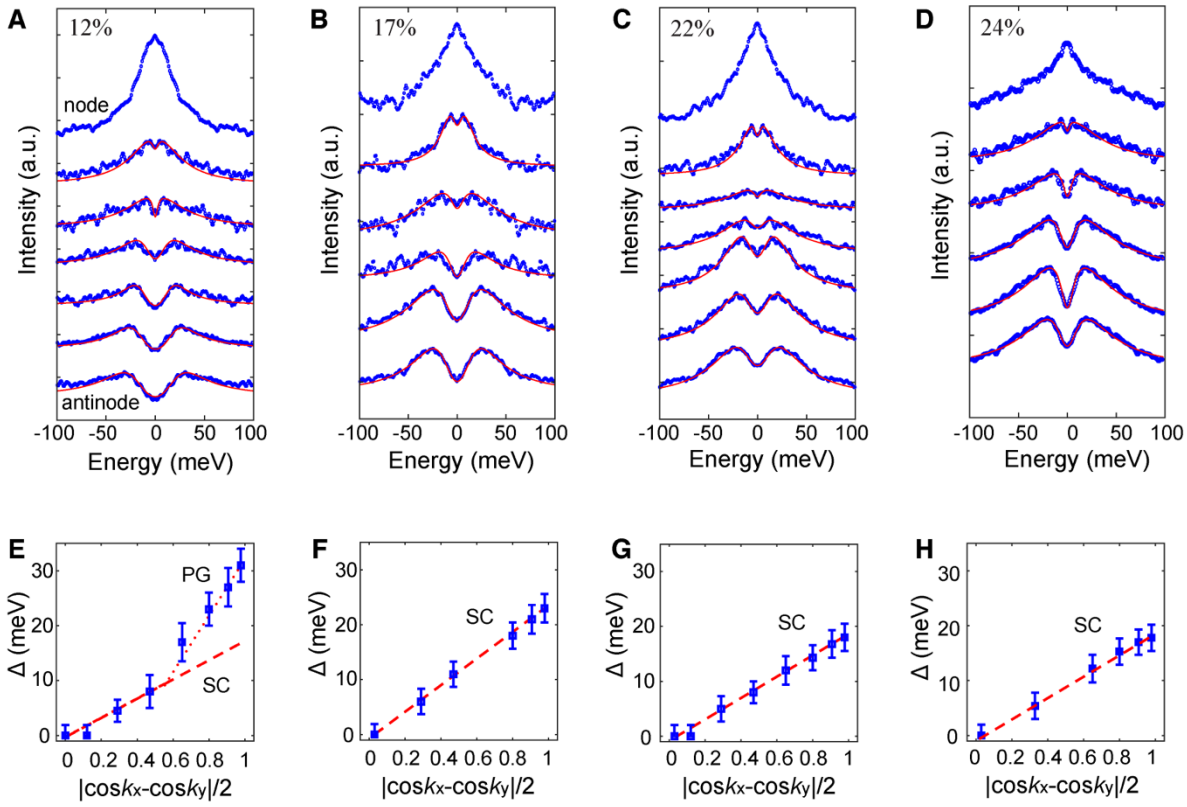

Fig. 4. **Superconducting gap symmetry.** (A-D) Angle-dependent and doping-dependent symmetrized EDCs at k_F's. The red lines are fittings to obtain the gap sizes. (E-H) Angle-dependent and doping-dependent gap sizes. Dashed red lines are guides for the *d*-wave paring symmetry. Dotted red line denotes the dominant contribution of pseudogap around antinodal regime. Error bars reflect the fitting uncertainty in determining Δ. Measurement temperature is 9 K.

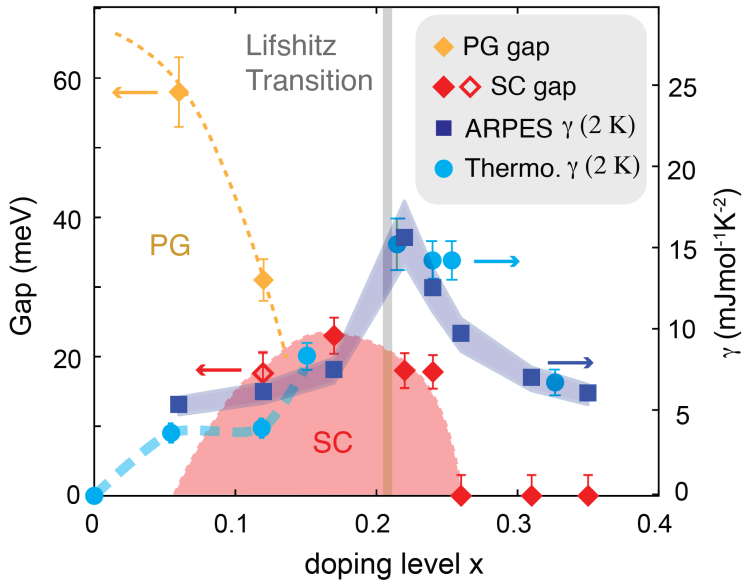

Fig. 5. **Doping-dependent electronic specific heat and phase diagram of LSCO.** Red solid diamonds are doping-dependent superconducting (SC) gaps. The open diamond corresponds to the extrapolated SC gap at 12% doping in Fig. 4E. Yellow diamonds correspond to the measured pseudogap in the underdoped regime. Error bars reflect the fitting uncertainty in determining Δ. Grey vertical area represent the Lifshitz transition range same as the range between x_1 and x_2 in Fig. 2C. Dark blue squares are electronic specific heat coefficients (γ) calculated for 2 K based on ARPES band structure parameters. Cyan circles are the thermodynamic electronic specific heat coefficients at 2 K by AC microcalorimetry from ref. 33. The shaded blue curve represents the upper and lower bounds to the calculated γ by considering the uncertainty of t_1 (175 – 205 meV). The uncertainty of γ caused by the t_z error of is ± 1 mJmol^{-1}K^{-2} (not shown in the figure). $t_z = 0.04t_1$ is used here based on the finding shown in Fig. 2. If $t_z = 0.07t_1$ would be used [30], the calcualted γ at $x = 0.22$ would become about 15% lower (shown in Fig. S6), which would not significantly change the agreement with thermodynamic measurements considering comparable error scales. The thick dashed cyan curve indicate the deviation of the thermodynamic results from spectroscopic data in the pseudogap regime.

SUPPLEMENTARY MATERIAL FOR

Differentiated roles of Lifshitz transition on thermodynamics and superconductivity in $La_{2-x}Sr_xCuO_4$

Yong Zhong[1,2,3†*], Zhuoyu Chen[1,3†*], Su-Di Chen[1,3], Ke-Jun Xu[1,3], Makoto Hashimoto[4], Yu He[5], Shin-ichi Uchida[6], Donghui Lu[4], Sung-Kwan Mo[2], and Zhi-Xun Shen[1,3*]

[1]*Stanford Institute for Materials and Energy Sciences, SLAC National Accelerator Laboratory, Menlo Park, CA 94025, USA*
[2]*Advanced Light Source, Lawrence Berkeley National Laboratory, Berkeley, CA 94720, USA*
[3]*Geballe Laboratory for Advanced Materials, Departments of Physics and Applied Physics, Stanford University, Stanford, CA 94305, USA*
[4]*Stanford Synchrotron Radiation Lightsource, SLAC National Accelerator Laboratory, Menlo Park, CA 94025, USA*
[5]*Department of Applied Physics, Yale University, New Haven, Connecticut 06511, USA*
[6]*Department of Physics, University of Tokyo, Tokyo 113-0033, Japan*

[*]Correspondence to: ylzhong@stanford.edu, zychen@stanford.edu, zxshen@stanford.edu
[†]These authors contributed equally.

The PDF file includes:

Text S1. LSCO thin film preparation and ARPES measurements.

Text S2. Doping level determination.

Text S3. Tight-binding model calculations and simulations.

Fig. S1. Characterization of LSCO thin films.

Fig. S2. Doping-dependent EDC and MDC curves.

Fig. S3. Photon energy dependent ARPES measurements.

Fig. S4. Comparison of x = 0.22 thin film and x = 0.22 single crystal.

Fig. S5. Angle-dependent density of states (DOS) in k-space.

Fig. S6. t_z-dependent density of states (DOS)

Fig. S7. Temperature dependent C_V/T.

Fig. S8. Influence of the disorder effect to DOS.

Table S1. Table of elemental fluxes for LSCO samples.

Table S2. Table of band structure parameters.

Supplementary Text

Text S1. LSCO thin film preparation and ARPES measurements.

The characterization of LSCO thin film is shown in Fig. S1. $LaSrAlO_4$ (001) substrate is chosen due to the relatively small lattice mismatch with LSCO. Before growth, the substrate is annealed in oxygen at 1000 ^oC with close contact to a $LaAlO_3$ substrate to ensure a AlO_2 termination. RHEED patterns and real-time oscillations demonstrate an atomic layer-by-layer growth mode. The horizontal spacing between diffraction streaks of epitaxial LSCO film is used to calibrate the size of Brillouin zone in ARPES measurements. Wide-angle X-ray diffraction measurements show a single phase in our films. Clear Kiessig fringers around main peaks reflect the high quality of the sample. The AFM image shows an atomically smooth surface.

ARPES measurements were performed at beamline 5-2 of the Stanford Synchrotron Radiation Lightsource. The chemical potential was calibrated by a polycrystalline gold film connected to the sample stage. Linearly polarized light with $h\nu = 70$ eV was used to map the evolution of in-plane Fermi surfaces and explore the superconducting gap symmetry. Doping-dependent EDC curves at antinode/node, and MDC curves at node are displayed in Fig. S2. Ageing effect is also explored by warming up the sample ($x = 0.26$) to 50 K and then cooled down to 9 K. EDC curves are recovered after this cycle, indicating negligible ageing effect in films. Photo-energy dependent ARPES measurements are carried out to access the information of out-of-plane Fermi surfaces. Higher photon energy covers a larger momentum space. Antinodal MDCs are used to extract the momenta k_B's, as shown in Fig. S3.

Text S2. Doping level determination.

We use the Luttinger theorem to determine the doping levels of LSCO thin films. The error bars are ± 1.5% estimated by the uncertainty of k_F's determination. Meanwhile, we also measure the elemental fluxes by quartz crystal microbalance (QCM) during growth. Both methods show a similar trend of x, as shown in Table S1. QCM displays a large deviation in heavily overdoped regime, indicating the Sr solution limit in LSCO thin film. In addition, we benchmark the doping level in $x = 0.22$ thin film by performing ARPES measurement with the identical experimental setup on a $x = 0.22$ single-crystal sample. Similar Luttinger volume, EDC curves, superconducting gap and interlayer hopping parameter k_z are found (Fig. S4).

Text S3. Tight-binding model calculations and simulations.

We use a three-dimensional tight binding model to calculate the DOS near Lifshizt transition and compare it with thermodynamic properties. Doping-dependent band structure parameters determined by ARPES measurements are listed on Table S2. Based on the parameters, angle-dependent DOS can be obtained in Fig. S5. Compared with the underdoped ($x = 0.12$) and heavily overdoped ($x = 0.35$) samples, the Fermi velocity (then the DOS) near the antinode in the Lifshitz transition range ($x = 0.22$) change dramatically. In

contrast, the DOS near the node seems to have no substantial variation. This means that the antinodal regime contributes mostly to the thermodynamic properties. Fig. S6 displays the t_z-dependent DOS. Three-dimensionality will dramatically flatten the DOS near the Lifshitz transition. Temperature-dependent specific heat is also calculated in S7. There is an obvious logarithmically divergent behavior at Lifshitz transition under the pure 2D limit. We also explore the influence of impurity scattering to the DOS near Lifshitz transition (Fig. S8). Although disorder lowers the DOS, our results are still available to interpret the specific heat data from experimental observations.

Table S1 **Table of elemental fluxes for LSCO samples.**

La $(2 \times 10^{13} atoms/ cm\text{^}2 * s)$	Sr $(2 \times 10^{13} atoms/ cm\text{^}2 * s)$	QCM x	Luttinger theorem x
1.01	0.02	3.9%	6%
1.01	0.05	9.4%	12%
1.01	0.08	14.6%	17%
1.01	0.1	18.0%	22%
1.01	0.12	21.2%	26%
1.01	0.22	39.2%	31%
1.01	0.32	48.1%	35%

Table S2 **Table of band structure parameters.**

x	t_1 (meV)	t_2 / t_1	t_3 / t_1	t_z / t_1	μ / t_1
6%	190	-0.16	0.08	0.04	-0.556
12%	190	-0.15	0.075	0.04	-0.66
17%	190	-0.144	0.072	0.04	-0.76
22%	190	-0.134	0.067	0.04	-0.805
24%	190	-0.132	0.066	0.04	-0.81
26%	190	-0.128	0.064	0.04	-0.826
31%	190	-0.12	0.06	0.04	-0.906
35%	190	-0.116	0.058	0.04	-0.99

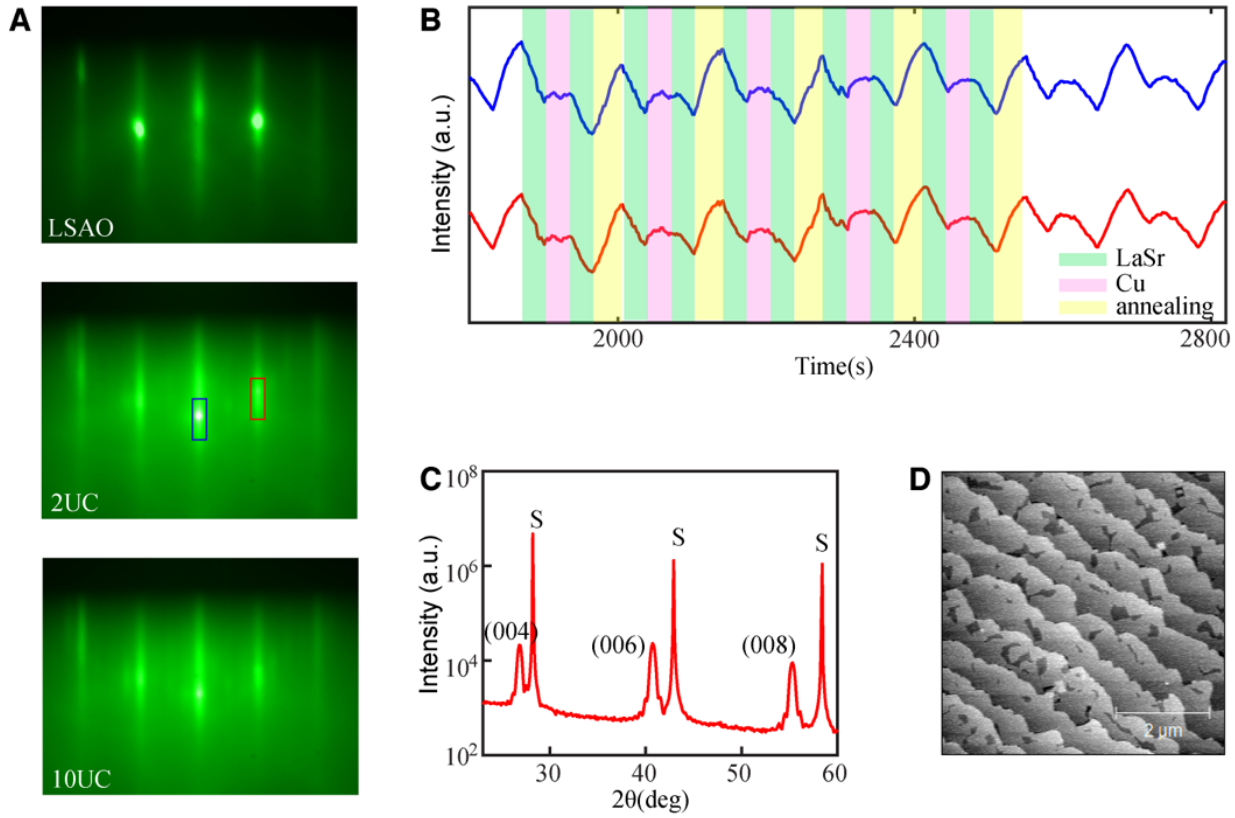

Fig. S1 Characterization of LSCO thin films. (A) RHEED patterns of $LaSrAlO_4$ (001) substrate (top), 2UC LSCO thin film (middle), and 10UC LSCO thin film (bottom). (B) Real-time RHEED intensity oscillations recorded during the growth process. Blue and red curves are intensity of (00) and (01) streaks labelled in the middle panel of (A). (C) Wide-angle X-ray diffraction scan of a 10UC LSCO thin film. (D) Atomic force microscopy image showing high quality of film surface.

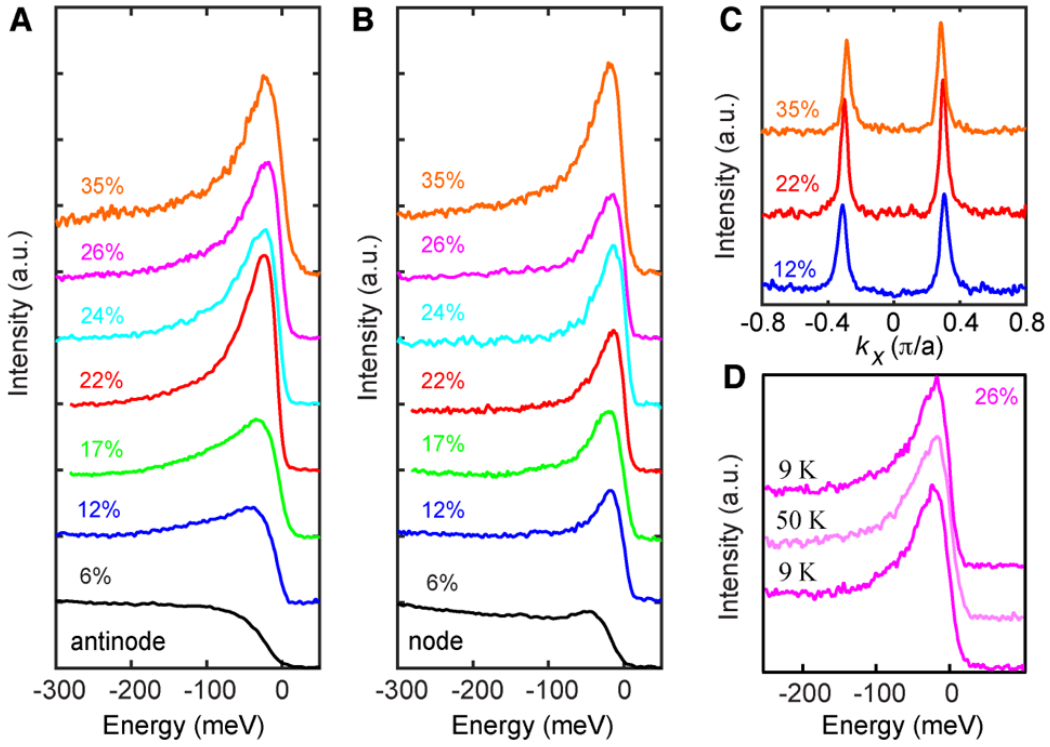

Fig. S2. Doping-dependent EDC and MDC curves. (A-B) Doping-dependent EDC curves at antinode/node. (C) Doping-dependent MDC curves along nodal direction. (D) Negligible ageing effect in LSCO thin films.

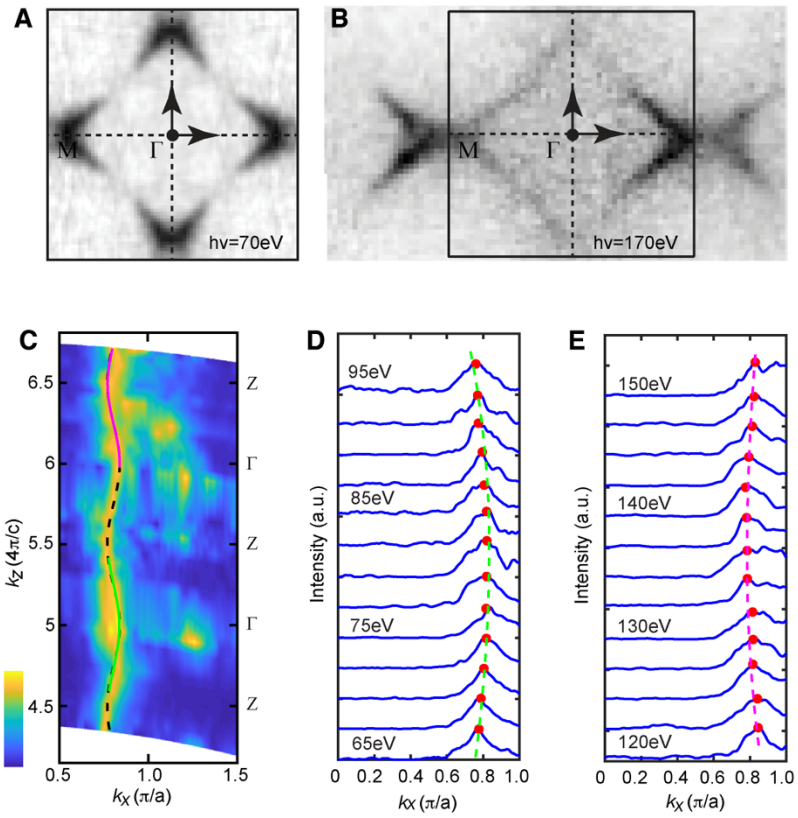

Fig. S3. Photon energy dependent ARPES measurements. (A-B) In-plane Fermi surfaces at photon energies $h\nu$ = 70eV, 170eV. (C) Out-of-plane Fermi surface maps along antinodal (π, 0) direction for x = 0.22 sample. (D-E) MDC curves at momenta k_B's in two energy ranges, 65 – 95 eV and 120 – 150 eV.

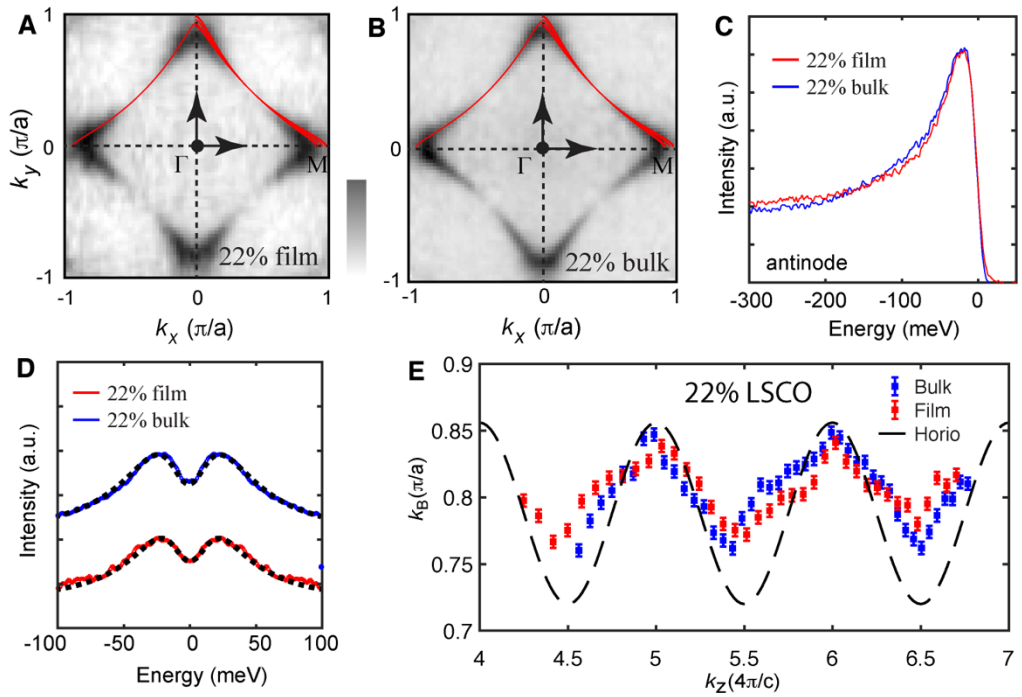

Fig. S4. Comparison of $x = 0.22$ thin film and $x = 0.22$ single crystal. (A-B) Fermi surface maps on $x = 0.22$ thin film and $x = 0.22$ single crystal. (C) Comparison of EDCs at antinode. (D) Comparison of symmetrized EDCs at antinode. (E) Similar interlayer hopping k_z.

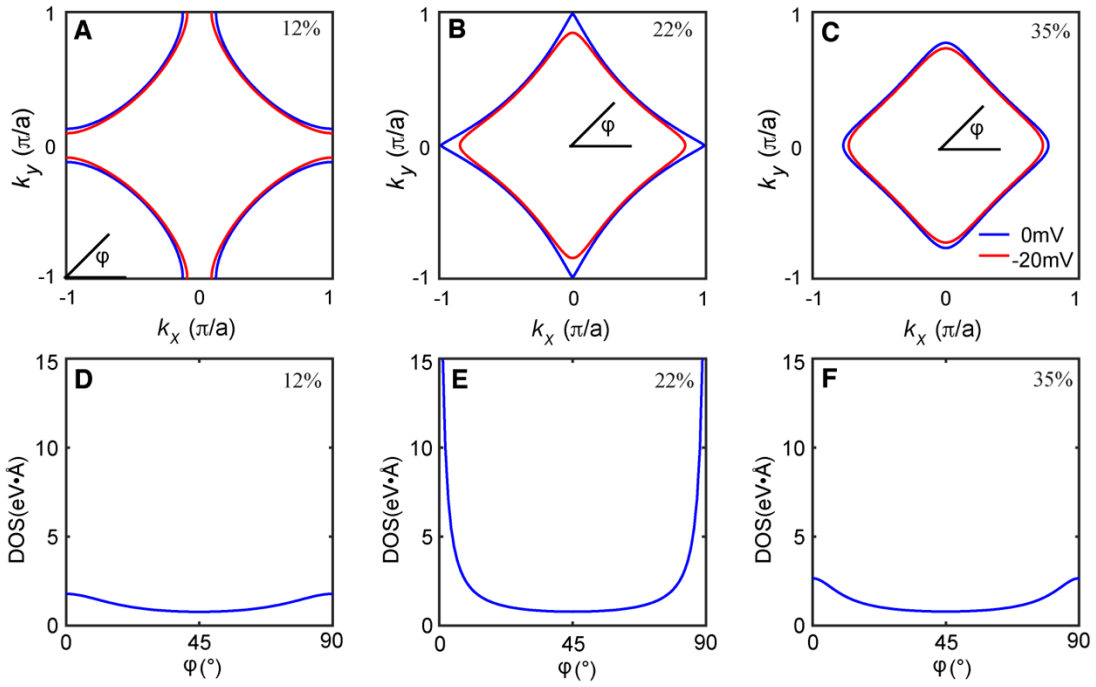

Fig. S5. Angle-dependent density of states (DOS) in k-space. (A-C) Energy contours (E = 0 meV, 20 meV) on x = 0.12, 0.22 and 0.35 samples. Azimuth angle φ is defined in the figures. (D-F) The corresponding angle-dependent DOS in momentum space.

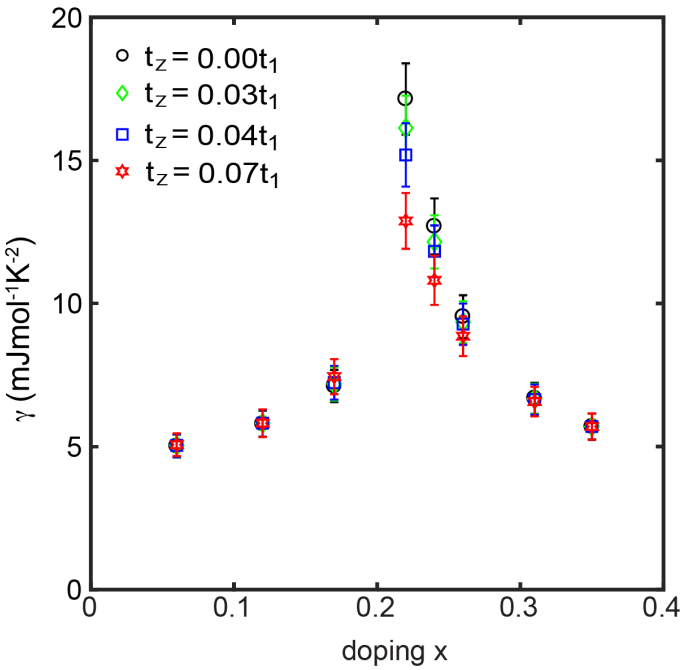

Fig. S6. Electronic specific heat coefficient γ at 2 K calculated with t_z = 0, 0.03 t_1, 0.04 t_1, and 0.07 t_1.

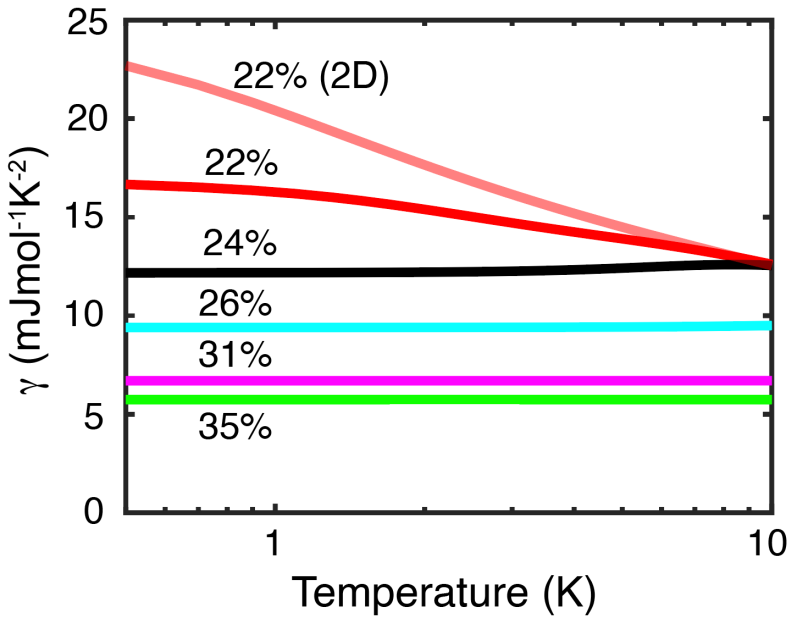

Fig. S7. Temperature-dependent electronic specific heat coefficient $\gamma = C_e/T$ calculated for overdoped LSCO samples. 2D van Hove singularity generates a $\log(1/T)$ dependence as temperature trends to zero.

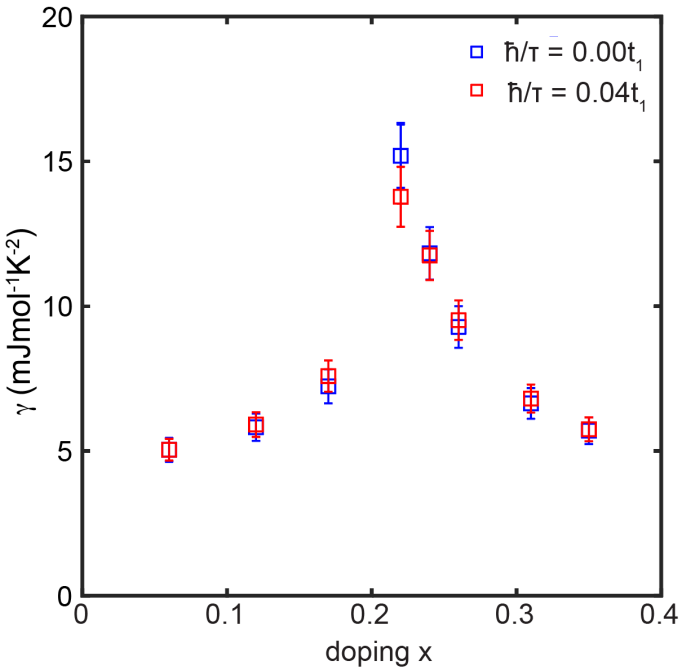

Fig. S8. Influence of the disorder effect to the electronic specific heat coefficient γ at 2 K**.** The same quasiparticle lifetime ($\hbar/\tau = 0.04\ t_1$) is used as ref. 31. Considering the disorder effect, the results are still consistent with microcalorimetry specific heat data in ref. 33 within experimental error.